Supplementary Information: Three-dimensional in-situ imaging of single-grain growth in polycrystalline films

Dmitry Dzhigaev,[1,*] Pierre-Alexis Repecaud,[2] Yury Smirnov,[2] Lucas Atilla Bernardes Marçal,[1] Giovanni Fevola,[3] Dina Sheyfer,[4] Quentin Jeangros,[5] Wonsuk Cha,[4] Ross Harder,[4] Anders Mikkelsen,[1] Jesper Wallentin,[1] Monica Morales-Masis,[2] and Michael Elias Stuckelberger[3]

[1]*Division of Synchrotron Radiation Research and NanoLund, Department of Physics, Lund University, P.O. Box 118, SE-221 00 Lund, Sweden*

[2]*MESA+ Institute for Nanotechnology, University of Twente, Enschede, 7500 AE, The Netherlands*

[3]*Centre for X-ray and Nano Science (CXNS), Deutsches Elektronen-Synchrotron DESY, Notkestraße 85, DE-22607 Hamburg, Germany*

[4]*APS, Argonne National Laboratory, 9700 S Cass Ave, Lemont, IL 60439, United States*

[5]*EPFL STI IMT PV-LAB, MC A2 238 (Bâtiment MC) Rue de la Maladière 71b, CP 526, CH-2002 Neuchâtel 2, Switzerland*

(Dated: December 22, 2021)

* dmitry.dzhigaev@sljus.lu.se

Set point [C°]	Calibrated temperature [C°]
20	20.09
50	54.05
100	99.04
150	154.21
200	208.07
250	266.80

TABLE S1. Temperature calibration of the heating cell. The T values in the main text are calculated by linear interpolation.

S1. TEMPERATURE CALIBRATION OF THE HEATER CELL

The values of temperature provided by the heater device thermocouple tend to differ from those of IZrO film. This discrepancy arises from the thermal resistance between the thermocouple (attached to the sample clip), and the thin film in the heating setup (see Figure S1). The calibration was done by using the known parameters of thermal expansion of a sapphire crystal. The substrate was sitting under N_2 flow with the flow rate of about 125 sccm. X-ray energy was 11.5 keV. The positions of the 006 Bragg peak were recorded as a function of temperature and actual temperature values of the crystal were recalculated (see Table S1).

S2. *IN SITU* SCANNING TRANSMISSION ELECTRON MICROSCOPY (TEM) AND ELECTRON BACKSCATTER DIFFRACTION (EBSD)

The frames extracted from movie of *in-situ* annealing of IZrO film similar to the one in the main text are presented in Figure S2a. High-resolution electron diffraction patterns are shown in Figure S2b,c. Electron Backscatter Diffraction (EBSD) images obtained from the same sample as in the main text are shown in Figure S3.

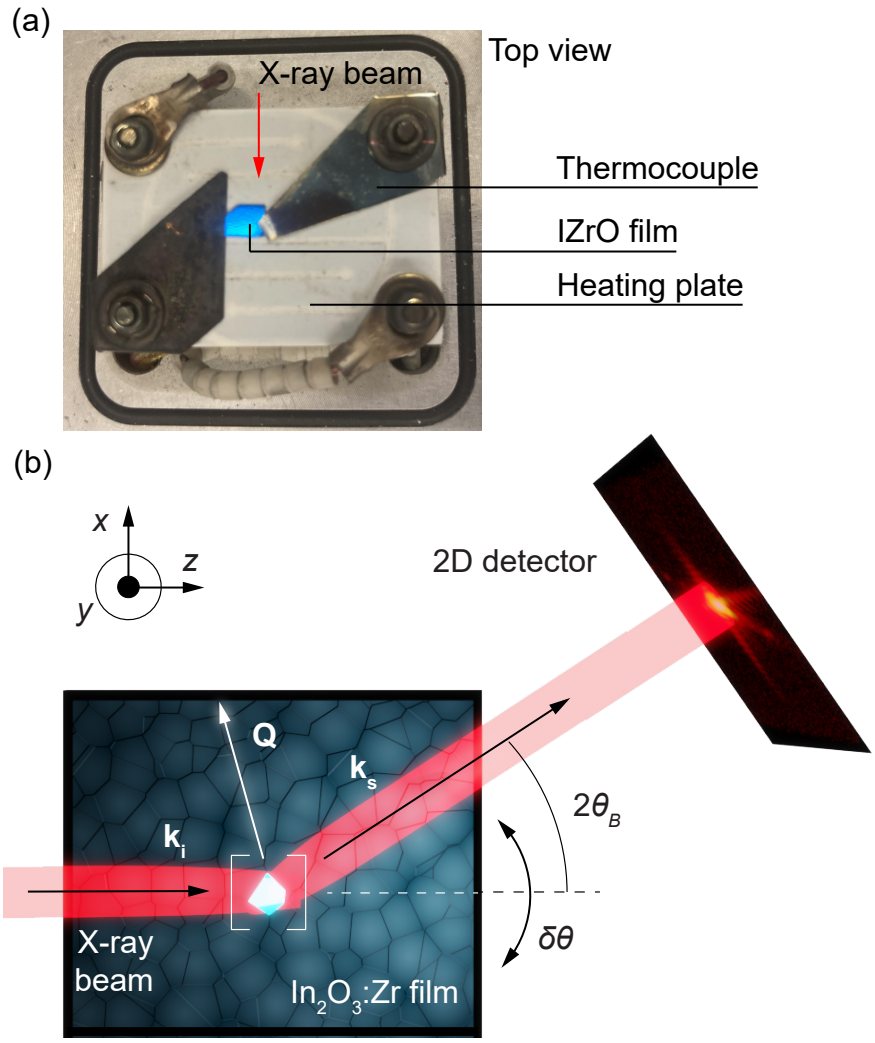

FIG. S1. (a) Top view over the heater sample cell. Thin film (blue) mounter onto heating plate and clamped with thermocouple contacts. (b) Scheme of Bragg coherent diffraction imaging experiment in the laboratory reference frame defined by xyz-axes. Coherent X-rays fully illuminate a single grain in In_2O_3:Zr and produce the Bragg peak measured at the 2D detector. The 3D diffraction patterns were obtained by recording intensities at the detector plane for a set of incidence angles $\delta\theta$ in the vicinity of (222) Bragg condition.

S3. RECIPROCAL SPACE ANALYSIS

First, the change of an average lattice spacing was evaluated. The **Q**-space coordinates were calculated for every pixel in the BCDI datasets and the center of mass (COM) of the Bragg peaks were retrieved as $\mathbf{Q}_{COM}$. The projections of the Q-space intensity distribution

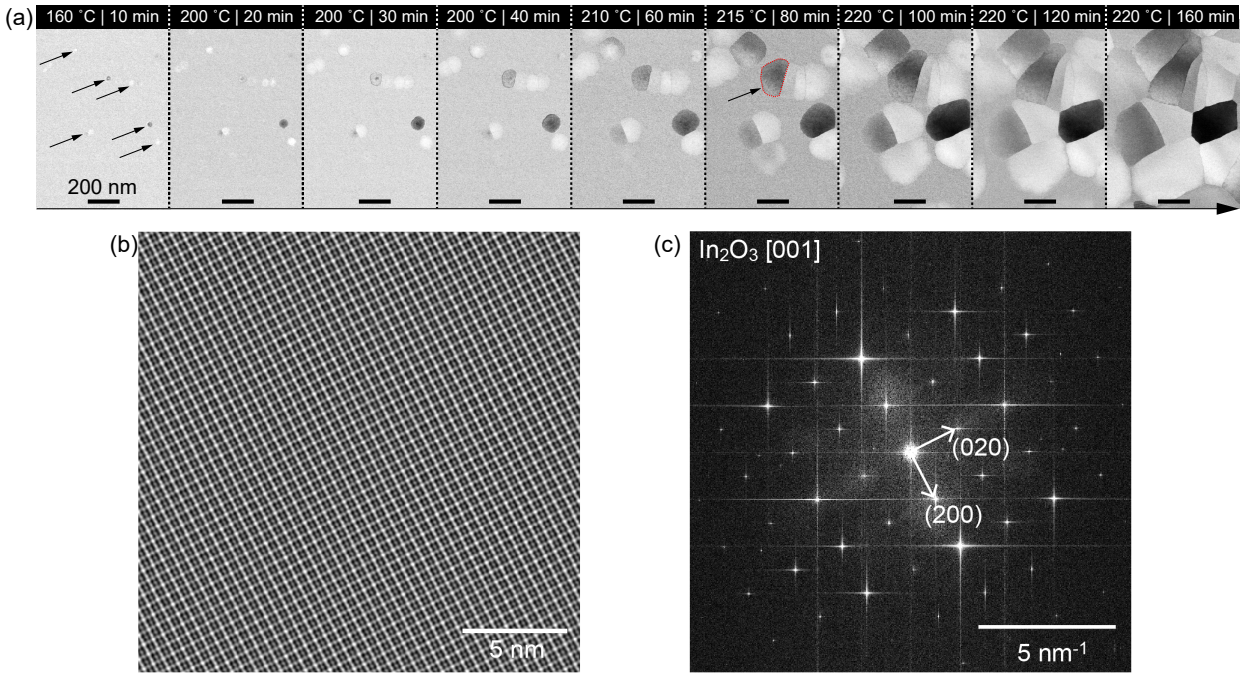

FIG. S2. (a) Transmission electron microscopy of IZrO film crystallization process as a function of time and temperature. The initial grains are shown by arrows in the first frame. The grain with the morphology similar to the one revealed by BCDI is shown by a red dashed line in the 80 min frame. (b) Atomic-resolution STEM high-angle annular dark-field (HAADF) image. (c) Corresponding fast Fourier transform of the In_2O_3 lattice after full crystallization of the film in the microscope.

are shown in Figure S4a for three time points. Periodic fringes arise from the shape of the grain and reveal its faceted structure.

The average lattice d-spacing was calculated as d=$2\pi/|\mathbf{Q}_{COM}|$ and the time dependencies are shown in Figure S4b. Here, we evaluate the relative strain change with respect to the final value in the time series, assuming it to be the final state of the TCO film. The curve shows a clear plateau toward the second half of data points, with a deviation of 2×10^{-4} for the last two points after 2 hours of annealing.

The sample was characterized by laboratory source X-ray diffraction (XRD) after the synchrotron experiment. The XRD pattern is collected using STOE STADI MP diffractometer with Cu anode X-ray source (voltage of 40 kV, current 40 mA) in reflective geometry. The scanning step width was 0.2° and the counting time 10 s per step. Typical size of the beam spot on the sample for STOE STADI MP diffractometer is 0.4×12 mm, therefore a

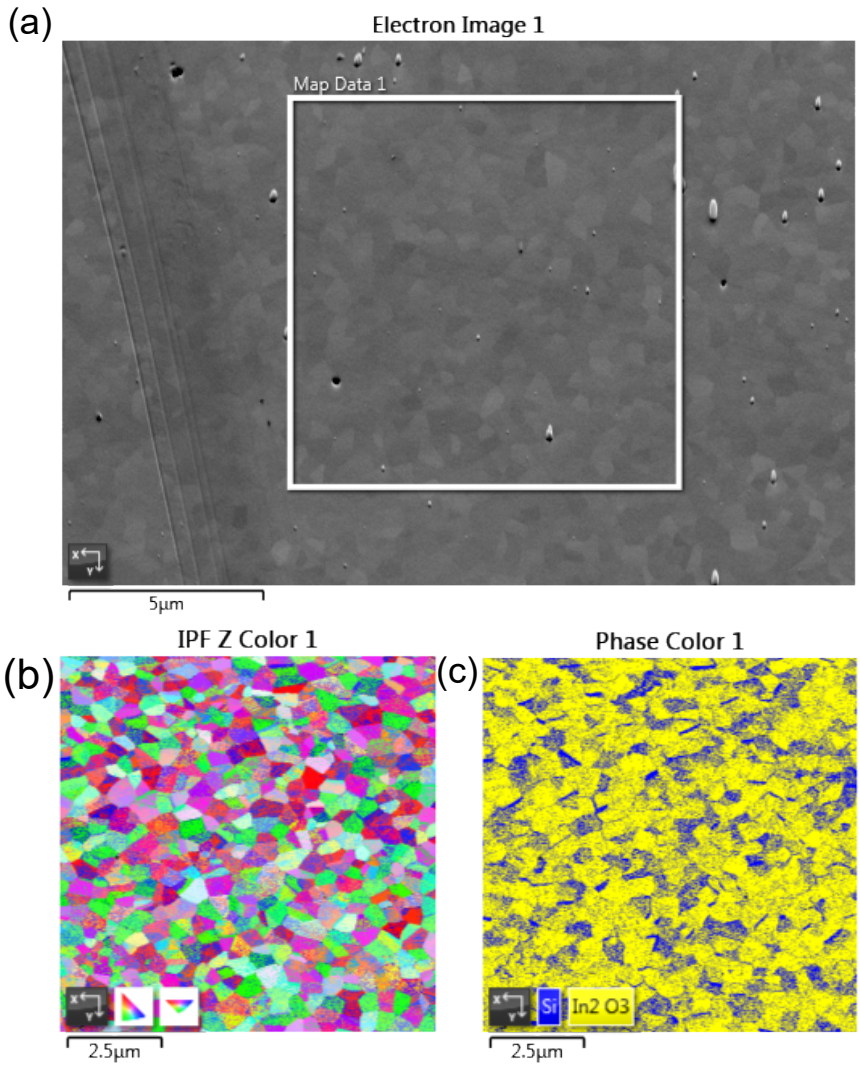

FIG. S3. Color plots from Electron Backscatter Diffraction (EBSD) measurements for IZrO film studied by BCDI in the main text. The following phase fractions were extracted: Si - 23.44 %, In_2O_3 - 76.15 %, and Zero solutions - 0.41 %.

considerable number of grains were illuminated to obtain their average structure and orientation. The DECTRIS MYTHEN 1K pixel detector gives a precise angular resolution of 0.03° FWHM. Post-beamtime XRD revealed the d spacing value of 2.8998 Å (see Figure S5). This value corresponds well to optimized *ex situ* annealing of In_2O_3 films reported earlier in Ref. [1].

The impact of the thermal expansion of IZrO lattice was estimated from the thermal expansion coefficients obtained for pure In_2O_3 [2]. The lattice parameter change is governed by second-order expansion $a(T) = a_0(1+\alpha T+\beta T^2))$, where $\alpha = 7.2{\cdot}10^{-6}$ and $\beta = 1.15{\cdot}10^{-9}$.

Assuming $T = 81°C$ the interplanar spacing d_{222}=2.9223 Å, which is $6 \cdot 10^{-4}$ increase with respect to table values.

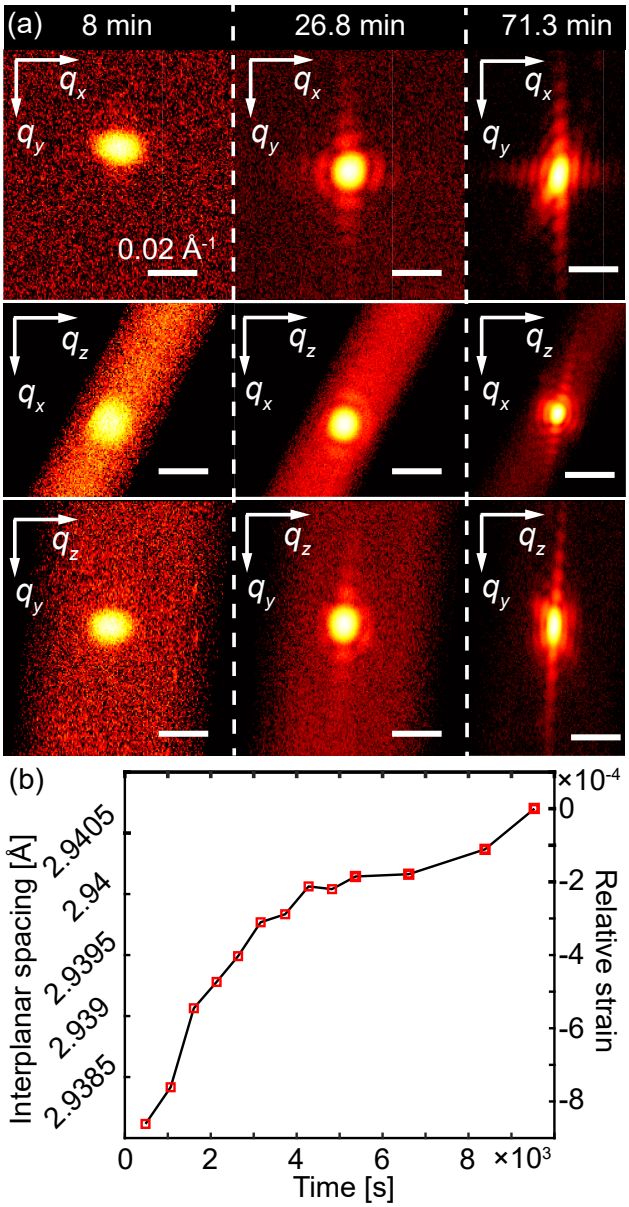

FIG. S4. (a) Three orthogonal projections of the reciprocal space intensity (log-scale) distribution in the vicinity of (222) Bragg peak of IZrO. The corresponding annealing time steps are shown at the top of the figure. (b) Average interplanar spacing d_{222} and strain evolution over the whole IZrO grain as a function of annealing time.

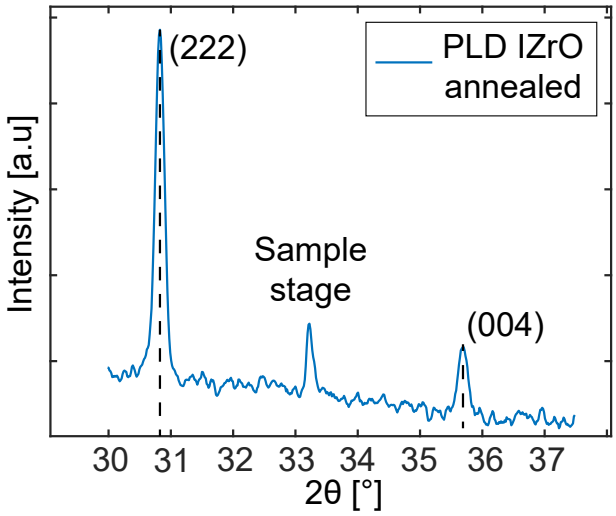

FIG. S5. X-Ray diffractogram of the annealed polycrystalline Zr-doped In_2O_3 film. The additional peak between (222) and (004) comes from the metallic sample stage.

S4. SCHERRER ANALYSIS

BCDI datasets from first few time steps could not be processed via phase retrieval due to the lack of coherent fringes. The reason for that is a comparably small volume of the grain at first stages of crystallization. The upper limit on the grain size was estimated by Scherrer equation [3]

$$S = \frac{K \cdot \lambda}{\beta \cdot \cos\theta_B} \tag{1}$$

Here, K=0.94 is a shape factor, λ is the wavelength of radiation, β is the broadening of the Bragg reflection at FWHM, and θ_B is Bragg angle. Orthogonal line profiles in Q-space distributions were analyzed (see Figure S4a). The value for out-of-plane grain size was estimated as S_y ≈75 nm, the in-plane size S_{xz} ≈55 nm. We can conclude that after 8 min of annealing process the seed crystallite reached the thickness of as-deposited amorphous film. Additionally it sets the limit of ≈50 nm on the IZrO particles size which can be reconstructed reliably with BCDI at a 3^{rd} generation synchrotron source.

S5. JOHNSON–MEHL–AVRAMI–KOLMOGOROV (JMAK) ANALYSIS

The original JMAK equation can be rewritten in the form [4]

$$\ln\left(-\ln\left[-F(t)\right]\right) = \ln K + n \ln t. \tag{2}$$

The values of K and n can be obtained by plotting $\ln(1/(1-F(t)))$ vs $\ln t$. The linear fit provides intercept of $\ln K$ and slope n (see Figure S6a). This model however is very simplistic and does not take into account asymmetric growth of grains in thin films. These limitations can be addressed by employing the concept of local Avrami exponent $n(F)$ [5]. The JMAK equation can be transformed as follows

$$n(F) = \frac{\partial \ln(-\ln[1-F(t)])}{\partial \ln t}. \tag{3}$$

The corresponding plot of $n(F)$ is show in Figure S6b.

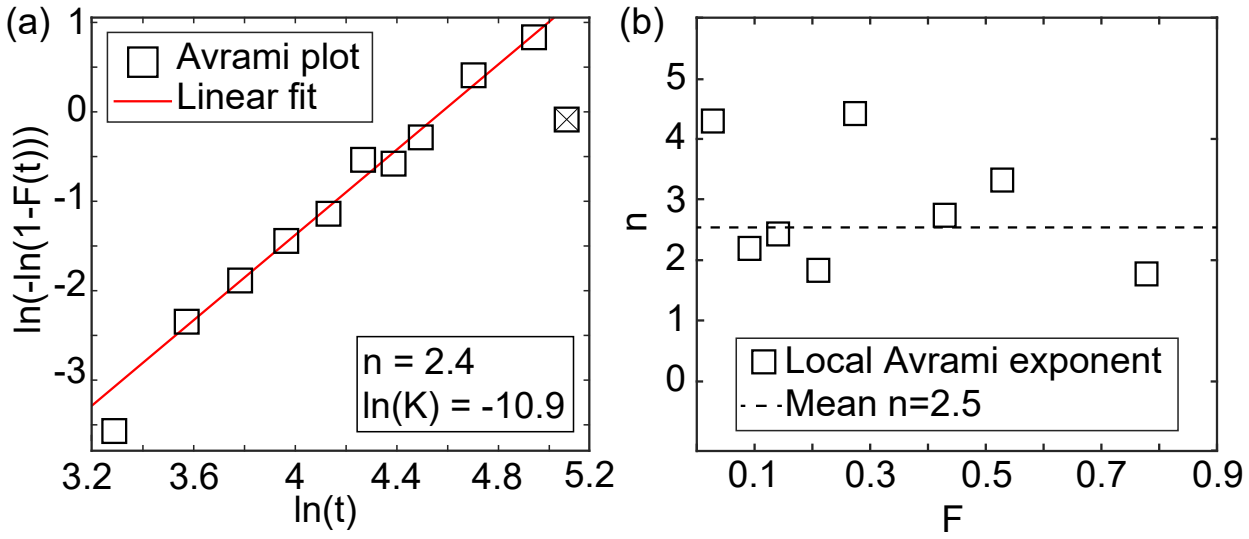

FIG. S6. (a) Avrami plot for the crystallization at 140 °C IZrO films grown by PLD. (b) Local Avrami exponent plot. In both panels outliers are marked with crosses.

S6. RESOLUTION ESTIMATION

We evaluated the real space resolution of the reconstruction by the edge response functions [6]. Profiles were extracted in the direction normal to facets of the particle and their profiles were averaged. The line spread function (LSF) was obtained by taking the derivative of the edge response.

[1] Junjun Jia, Shimpei Iwasaki, Shingo Yamamoto, Shin-ichi Nakamura, Eisuke Magome, Toshihiro Okajima, and Yuzo Shigesato. Temporal evolution of microscopic structure and function-

ality during crystallization of amorphous indium-based oxide films. *ACS Applied Materials & Interfaces*, 13(27):31825–31834, 2021.

[2] K. D. Kundra and S. Z. Ali. Thermal expansion of In_2O_3. *Journal of Applied Crystallography*, 3(6):543–545, Dec 1970.

[3] AL Patterson. The scherrer formula for x-ray particle size determination. *Physical review*, 56(10):978, 1939.

[4] Ajay Kumar Jena and Mahesh Chandra Chaturvedi. *Phase transformation in materials*. Prentice Hall, 1992.

[5] A Calka and AP Radlinski. The local value of the avrami exponent: a new approach to devitrification of glassy metallic ribbons. *Materials Science and Engineering*, 97:241–246, 1988.

[6] D Dzhigaev, A Shabalin, T Stankevič, U Lorenz, RP Kurta, F Seiboth, J Wallentin, A Singer, S Lazarev, OM Yefanov, et al. Bragg coherent x-ray diffractive imaging of a single indium phosphide nanowire. *Journal of Optics*, 18(6):064007, 2016.